Author Manuscript

Author Manuscript

Author Manuscript

Author Manuscript

HHS Public Access
Author manuscript
Nat Chem Biol. Author manuscript; available in PMC 2021 January 07.

Published in final edited form as:
Nat Chem Biol. 2020 October ; 16(10): 1087–1095. doi:10.1038/s41589-020-0565-2.

Spectroscopic coherent Raman imaging of *Caenorhabditis elegans* reveals lipid particle diversity

Wei-Wen Chen[1,2], **George A. Lemieux**[3], **Charles H. Camp Jr**[2], **Ta-Chau Chang**[4], **Kaveh Ashrafi**[3,✉], **Marcus T. Cicerone**[1,2,✉]

[1]School of Chemistry & Biochemistry, Georgia Institute of Technology, Atlanta, GA, USA.

[2]Biosystems and Biomaterials Division, National Institute of Standards and Technology, Gaithersburg, MD, USA.

[3]School of Medicine, University of California, San Francisco, CA, USA.

[4]Institute of Atomic and Molecular Sciences, Academia Sinica, Taipei, Taiwan.

Abstract

Caenorhabditis elegans serves as a model for understanding adiposity and its connections to aging. Current methodologies do not distinguish between fats serving the energy needs of the parent, akin to mammalian adiposity, from those that are distributed to the progeny, making it difficult to accurately interpret the physiological implications of fat content changes induced by external perturbations. Using spectroscopic coherent Raman imaging, we determine the protein content, chemical profiles and dynamics of lipid particles in live animals. We find fat particles in the adult intestine to be diverse, with most destined for the developing progeny. In contrast, the skin-like epidermis contains fats that are the least heterogeneous, the least dynamic and have high triglyceride content. These attributes are most consistent with stored somatic energy reservoirs. These results challenge the prevailing practice of assessing *C. elegans* adiposity by measurements that are dominated by the intestinal fat content.

It is possible to form an image of a biological specimen by obtaining a Raman spectrum at each image pixel. Through intrinsic molecular vibrations, Raman spectra report on all chemical species present at moderate and high concentration, including lipids, proteins, sugars and small molecules. Raman spectra of biological systems generally contain ~45

Reprints and permissions information is available at www.nature.com/reprints.

✉**Correspondence and requests for materials** should be addressed to K.A. or M.T.C. Kaveh.Ashrafi@ucsf.edu; cicerone@gatech.edu.

Author contributions
K.A., T.-C.C., M.T.C. and W.-W.C. initiated the project. G.A.L., K.A. and W.-W.C. conceived and designed the study. W.-W.C. conducted all experiments. C.H.C. and W.-W.C. developed the ensemble machine-learning workflow. W.-W.C. analyzed all data with discussions and contributions from G.A.L., K.A., M.T.C., C.H.C. and T.-C.C. G.A.L. and K.A. conceived and drew Fig. 6. W.-W.C., G.A.L., K.A. and M.T.C. wrote the manuscript. All authors reviewed the manuscript.

Competing interests
The authors declare no competing interests.

Additional information
Extended data is available for this paper at https://doi.org/10.1038/s41589-020-0565-2.

Supplementary information is available for this paper at https://doi.org/10.1038/s41589-020-0565-2.

Author Manuscript Author Manuscript Author Manuscript Author Manuscript

chemical bond-specific peaks in the ‘fingerprint’ spectral region(from 500 to 1,800 cm^{-1}). These peaks are weak, but highly informative. Another five, much stronger peaks (10× to 100×) are found in the ‘CH stretch’ region (from 2,800 to 3,000 cm^{-1}). Together, these ~50 spectral peaks provide information regarding even subtle chemical variations such as differences in degree of saturation or esterification of lipids. Thus, spectroscopic Raman imaging provides extremely rich spatial and chemical information without any labeling. Inspite of its transformative potential for biological imaging, and although it was introduced decades ago[1], spectroscopic Raman imaging has not found widespread use in biology because it is far too slow, requiring seconds or minutes to acquire each spectrum[2], and thus each image pixel.

Coherent Raman imaging (CRI) methods shorten the time needed for acquiring the Raman signal[3]. However, most CRI techniques, such as narrow-spectrum coherent anti-Stokes Raman scattering (CARS) and stimulated Raman scattering (SRS), acquire the Raman signal only in a narrow portion of the strong CH stretch region and thus can discriminate only between water, protein and lipid, without the ability to further sub-classify[3]. A few studies that make use of these CRI techniques[4–6] have utilized a moderate spectral range (usually <400 cm^{-1}) in the fingerprint region. However, image acquisition times for full spectral imaging using these methods remain prohibitive[3].

We recently developed a broadband coherent anti-Stokes Raman scattering (BCARS) imaging platform that acquires robust fingerprint and CH-stretch Raman spectra at each laser pulse, largely bringing to fruition the potential of CRI methods for revealing the complexity of biological systems[3]. BCARS overcomes the problem of the weak fingerprint response by using a highly efficient signal generation paradigm[7] and by using the so-called ‘non-resonant background’ (NRB) as a phase-locked local oscillator for heterodyne signal amplification[8]. Ironically, the NRB had been universally viewed as a nuisance and caused many to abandon CARS for SRS[9]. Under favorable conditions it is sometimes possible to acquire fingerprint signals without utilizing the NRB; however, to retrieve an undistorted Raman spectrum the NRB must be properly accounted for[7,8] and this requires broad spectral acquisition. When used properly, the NRB simultaneously acts as a robust amplifier of small signals and as an internal reference, yielding Raman spectra with absolute peak heights and ratios[10]. With optimal NRB utilization, the BCARS system acquires micrographs with 500-nm spatial resolution at 3.5 ms per pixel, with each pixel containing a high-quality, intrinsically calibrated Raman spectrum covering the range 600 cm^{-1} to >3,100 cm^{-1} (ref. [7]). It provides rapid, label-free and non-invasive imaging with good chemical sensitivity and excellent, highly repeatable chemical specificity for biological samples.

The fat content in *Caenorhabditis elegans* is an especially interesting target for highly specific chemical imaging and has often been used as a way of demonstrating the applicability of CRI methods to biological systems[4–6,11–17]. Counterparts of many of the neural, endocrine and metabolic pathways known to affect *C. elegans* fat also play roles in the regulation of fat content in mammals[18,19]. Thus far, the fat content of *C. elegans*, whether measured by traditional histochemical staining, biochemical measurement of extracted lipid or by narrow-spectrum CRI, has been generally assumed to represent the stored somatic energy reservoir. Therefore, changes in overall *C. elegans* fat content have

Author Manuscript

Author Manuscript

Author Manuscript

Author Manuscript

been interpreted as changes in adiposity[20–22]. However, known physiological differences between *C. elegans* and mammals suggest that this assumption may not be accurate. Lacking anatomically defined adipocytes, the vast majority of somatic fat deposits in *C. elegans* occur in its intestinal and skin-like epidermal cells, with the intestinal cells being the major fraction of the overall volume in the organism's soma and where ~90% of somatically deposited lipids are found[11]. Importantly, the intestine of a *C. elegans* hermaphrodite is the production site of yolk—ApoB-like lipoprotein particles that transfer lipids and other nutrients to the developing oocytes within the hermaphrodite gonad[23]. In principle, changes in *C. elegans* fat content may reflect changes to mechanisms of energy storage and utilization, changes to mechanisms involved in lipid distribution to the progeny, or both. The ability to distinguish among the different types of fat deposit that play physiologically distinct functions is therefore critical to accurate interpretation of measurements of *C. elegans* fat content and usage.

Here, we apply BCARS to an in-depth in vivo study of the composition, tissue distribution and dynamics of lipid-rich structures in *C. elegans*. Our findings suggest that a significant fraction of lipids in the intestinal cells of hermaphrodites are destined for the embryo and thus cannot be considered as the equivalent of fat storage in the hermaphrodite mother.

Results

Lipid particles in *C. elegans* are chemically diverse.

We identified lipid-rich deposits in *C. elegans* by CARS microscopy using the 2,845-cm^{-1} resonance. We simultaneously acquired CARS and two-photon excitation fluorescence (TPE-F) images of fixed animals stained with LipidTOX, a neutral lipid-selective fluorescent dye, and statistically determined a 2,845-cm^{-1} significance threshold based on co-localization of these signals (Supplementary Fig. 1a,c). Particles with CARS 2,845-cm^{-1} intensity above this threshold are hereafter referred to as lipid-rich particles. The size distribution of lipid-rich particles in anesthetized, live animals imaged by CARS was similar to that of formalin-fixed animals that were imaged within 30 min. However, in animals at 24 h post-fix, the distribution skewed larger, suggesting that long-term formaldehyde fixation distorts the morphological characteristics of the particles (Supplementary Fig. 1b). This is significant, because commonly used histochemical techniques for visualizing *C. elegans* fat utilize formalin fixation[24,25].

Using CARS, we quantified lipid-rich particles in unfixed, anesthetized larval and adult animals in the intestine, epidermis and gonad (Supplementary Fig. 2a,b). In the intestine, lipid-rich particles steadily accumulate, peaking in the late L4 stage, then diminish in the adult stages (Supplementary Fig. 2b). By contrast, the lipid signal in the epidermis and the gonad is stable during larval development, then increases modestly in adulthood (Supplementary Fig. 2b). These findings suggest that the fat deposits in these three tissues may have different physiological functions.

We next compared spectral imaging results from several regions of the intestine in young, adult hermaphrodites (Fig. 1a–c). Spectra (600–3,100 cm^{-1}) from lipid-rich objects in these image regions revealed significant chemical heterogeneity (Fig. 1b,c). Almost all of the

Author Manuscript

Author Manuscript

Author Manuscript

Author Manuscript

lipid-rich particles contained unsaturated lipids (C=C, at 1,635– 1,650 cm^{-1}; Fig. 1d,e). The relative abundance of unsaturated to saturated bonds was not uniformly distributed between and within different particles (Fig. 1g). We found that some particles (Fig. 1a–c, regions of interest (ROIs) 3 and 4) contain both lipid (~2,845 cm^{-1}) and abundant protein signature signals including amide I stretching (1,665–1,680 cm^{-1}) and phenylalanine ring breathing (1,002 cm^{-1}). The overlaid 1,665–1,680 cm^{-1} and 2,845 cm^{-1} signals revealed the existence of numerous particles that exhibited both lipid and protein signals (Fig. 1f), along with particles in which either one signal or the other was dominant.

We quantitatively analyzed the lipid-rich droplets by first identifying object boundaries using the watershed approach[26] with the previously determined 2,845 cm^{-1} intensity threshold setting the minimum level of flooding. Once these objects were defined, we calculated the ratio of protein (1,665–1,680 cm^{-1}) to lipid (2,845 cm^{-1}) signals for each particle (Fig. 2a). Because the Raman shift of the amide I band varies depending on protein structure (~1,655 cm^{-1} in an a-helix and ~1,670 cm^{-1} in a β-sheet), we confirmed that the intensity of the 1,665–1,680 cm^{-1} region was strongly and positively correlated to that of the phenylalanine peak at 1,002 cm^{-1} (Pearson correlation coefficient = 0.74). In contrast, the correlation between the intensity of the 1,635–1,650 cm^{-1} region (due to the C=C stretch) and that of 1,002 cm^{-1} was weak (Pearson correlation coefficient = 0.19) (Supplementary Fig. 3a). Furthermore, as a control, we measured the protein-related signals (1,002 cm^{-1} and 1,665–1,680 cm^{-1}) in the body wall muscles of early L4 and adult worms and found that the intensity of these signals was invariant with development in this tissue (Supplementary Fig. 3b).

The heat map image of the protein:lipid ratio in Fig. 2a shows a variety of lipid-rich particles in the young adult intestine. We found that smaller particles were relatively high in protein content with a uniform protein:lipid ratio throughout the particle, while larger particles (typical diameter >2.5 μm) exhibited a low protein:lipid ratio with the lipids enriched in the core and the proteins on the edges. The smaller-sized, protein-rich lipid particles were predominantly found in the intestines of gravid hermaphrodites (Fig. 2a,b). At all developmental stages the epidermis almost exclusively contained lipid-rich but low-protein-content particles. In larval stage L3 and in early L4, the vast majority of particles within the intestine were similarly lipid-rich but protein-poor. However, beginning in late L4 larvae, particles characterized by higher protein content begin to dominate the intestinal population (Fig. 2b). This shift in protein content coincides with the L4-stage onset of germ cell proliferation[27] when the intestine commences yolk synthesis to transfer lipids and other nutrients from the parent to the developing oocytes[28]. We hypothesized that the small, protein-rich lipid particles that appeared at this time were related to yolk production.

Common GFP markers stain only subsets of lipid particles.

Following synthesis in the intestine, yolk particles are secreted into the pseudocoelom, a fluid-filled cavity that surrounds the gonad. Pseudocoelomic yolk particles are endocytosed by the developing oocytes[29]. As a reference point, we imaged transgenic worms that express VIT-2::GFP, a fusion protein widely used as a marker of yolk[29]. As expected, most of the VIT-2::GFP signal was observed in either oocytes or in deposits in the pseudocoelom of

Author Manuscript

Author Manuscript

Author Manuscript

Author Manuscript

gravid hermaphrodites. Within the pseudocoelom, the VIT-2::GFP signal co-localized with the CARS lipid signal (2,845 cm^{-1} resonance) (Supplementary Fig. 4a,b). The average protein:lipid ratio of these pseudocoelomic deposits (0.67 ± 0.09, mean ± s.d.) was similar to that of the highest protein:lipid ratio particles of the intestine. Although *vit-2* is known to be robustly expressed only by the intestines of hermaphrodites starting in L4[30], we detected very little VIT-2::GFP in these cells (Supplementary Fig.4a) after using spectral-or time-gated fluorescence capture to reject the autofluorescent background. Although protein-rich lipid particles were found throughout the intestine, co-localization with the VIT-2::GFP signal was largely restricted to the basolateral surface (Supplementary Fig. 4b), presumably a region from which yolk exits the intestine. Thus, within the intestine, the VIT-2:GFP marker may only be suitable for detecting yolk particles just prior to export but unsuitable for illuminating earlier steps in yolk formation. In oocytes, the CARS 2,845 cm^{-1} and VIT-2::GFP signals infrequently co-localized (Supplementary Fig. 4c), suggesting that most of the VIT-2::GFP-containing particles are delipidated post endocytosis.

DHS-3::GFP has been considered a marker of lipid droplets[31]. Approximately 80% and 60% of the intestinal lipid-rich, protein-poor particles in the intestines of late L4 and young adult stages, respectively, were ringed by DHS-3::GFP (Supplementary Fig. 4d). However, ~40% of DHS-3::GFP-positive particles failed to co-localize with a significant lipid-rich CARS resonance (Supplementary Fig. 4e). Moreover, while both the epidermis and the intestine contain lipid-rich but protein-poor particles, only the intestinal particles were labeled by DHS-3::GFP. Thus, although DHS-3::GFP can localize to lipid-rich particles, its utility as a proxy of fat storage depots is fraught with uncertainties.

Diverse lipid particles exhibit distinct flux dynamics.

Our findings suggest that the small, protein-rich lipid particles may be involved in lipid transport, akin to mammalian lipoproteins, while the large, protein-poor lipid particles may have energy storage functions akin to mammalian lipid droplets. Lipid particles that store energy would be expected to have a lower turnover rate than particles involved in lipid trafficking out of the soma to progeny. Therefore, we sought to determine the kinetics of lipid flux through these different particles. Carbon–deuterium bonds exhibit a distinctive CARS resonance at ~2,100 cm^{-1}, within a Raman frequency range uncluttered by resonances from most endogenous biomolecules[6], thus enabling CRI-based pulse-chase experiments using deuterated fatty acid (dFA) tracers. To assess dFA uptake kinetics, young adult *C. elegans* were fed OP50 *Escherichia coli* supplemented with either deuterated oleic acid or unlabeled oleic acid as a control for 2–12 h. They were then immediately BCARS imaged to quantify the relative abundance of C–D bonds (2,100 cm^{-1}) versus C–H bonds (2,850 cm^{-1}) (Supplementary Fig. 5a). After 4 h of feeding dFA, the C–D signal appeared, concentrated on the surface of a majority of the lipid-rich particles in the intestine. At longer time intervals of dFA feeding, the C–D signal distributed throughout the particles (Supplementary Fig. 5a), increased in intensity (Supplementary Fig. 5b) and particle coverage (Supplementary Fig. 5c). After 12 h of exposure, all of the lipid-rich particles in the animal contained the deuterium probe. To assess the turnover of assimilated lipids, we placed young adult *C. elegans* that had been fed dFA for 12 h, beginning at the late L4 stage, on OP50 lawns that lacked the deuterium label. Initially, all lipid-rich structures in the

Author Manuscript

Author Manuscript

Author Manuscript

Author Manuscript

intestine, epidermis and gonad exhibited a C–D signal (Fig. 3a). After 24 h of feeding on food lacking dFA, almost all the C–D signal at 2,100 cm^{-1} vanished from lipid-rich structures of the gonad (Supplementary Fig. 6a), consistent with the high flux of eggs (4–10 per hour) out of hermaphrodites[32]. Similarly, only a small fraction of the original C–D signal could be detected in the intestine after the 24-h chase (Fig. 3a). However, in the epi-dermis, ~86% of lipid-rich particles still presented a significant C–D signal, revealing the very different lipid flux kinetics of these tissues (Fig. 3a). The average 2,845 cm^{-1} intensity of the lipid-rich particles was the same among worms with different chase time points (Supplementary Fig. 6b), suggesting that the dFA is present at relatively small amounts and does not significantly displace endogenous lipids. The plots of dFA signals at chase intervals of 8, 12, 24 and 30 h were fit with an exponential decay curve (Fig. 3b). The characteristic decay time in the epidermis is ~20 ± 4 h, almost twice that of the intestine at ~11 ± 3 h.

To further quantify the lipid flux dynamics, we exploited BCARS fingerprint sensitivity to generate dFA:lipid (CD:CH) and protein:lipid (protein:CH) ratio heat maps by extracting the 2,100 (C–D), 2,845 (C–H) and 1,665–1,680 (protein) cm^{-1} signals from the acquired image data (Fig. 4a). Consistent with a slower loss of deuterium signal (Fig. 3b), after a chase of 24 h, the CD:CH ratio was much higher in the epidermis than in the intestine. We then examined the correlation between the CD:CH and protein:CH ratios for all lipid-rich particles (Fig. 4b). In the intestine, we found an obvious positive correlation between these two ratios after 8 h of dFA feeding, suggesting that the particles with abundant protein accumulate dFA more rapidly than the protein-poor particles. At 24 h of chase the correlation was inverted, indicating that the protein-rich particles lost dFA more quickly than the protein-poor particles. At the intermediate time point (12 h of dFA feeding = 0 h chase), no obvious positive correlation was observed, perhaps due to the increase of deuterium signal in the protein-poor particles, saturation of dFA accumulation in the protein-rich particles or both. The more chemically homogeneous epidermal lipid deposits lost the dFA label in a more uniform manner (Fig. 4b). These findings are consistent with protein-rich particles having a transitory lipid distribution role and protein-poor particles having a lipid storage role.

Diverse lipid particles have a distinct chemical make-up.

To determine whether yolk particles are spectroscopically distinguishable from the dFA-retaining particles, we obtained Raman spectra of the *C. elegans'* yolk. Mutation of *rme-2*, which encodes a low-density lipoprotein-like receptor expressed in the germline, results in defects in endocytosis of yolk particles but not in yolk production[29]. As a result, the *rme-2* mutants accumulate substantial amounts of lipoprotein deposits in their pseudocoelomic space[17]. These deposits, referred to as pseudocoelomic lipoprotein particles (PLPs), are much larger in size than yolk particles and are probably formed by the coagulation of numerous such yolk particles. The long-term dFA-retaining lipid-rich particles exhibited markedly different spectra than the PLPs (Supplementary Fig. 7a). The long-term dFA-retaining depots exhibited high levels of triglycerides signified by the strong resonances at 1,740 cm^{-1} and 2,845 cm^{-1}, which are characteristic of the ester carbonyl group and the CH_2 symmetric stretching respectively. The spectra of these particles showed little evidence of protein, lacking a detectable phenylalanine resonance at 1,002 cm^{-1} or a strong amide I

Author Manuscript

Author Manuscript

Author Manuscript

Author Manuscript

resonance at 1,665–1,680 cm^{-1}. By contrast, the PLP deposits exhibit strong pro tein and lipid signatures (CH_3 symmetric stretch at ~2,925 cm^{-1} and CH_2 symmetric stretch at ~2,850 cm^{-1}). Furthermore, PLP deposits lack the ester carbonyl resonance at 1,740 cm^{-1}, but exhibit a broad, complex peak from 1,600 cm^{-1} to 1,680 cm^{-1}. This peak may be due to several overlapping signals: unsaturated carbon–carbon bonds at ~1,650 cm^{-1}, amide I resonance at ~1,665 cm^{-1} and free fatty acid carbonyls resonating at ~1,645 cm^{-1} (ref. [33]). Cholesterol/cholesterol esters (700 cm^{-1}) were not detectable in either type of particle, in agreement with previous measurements by gas chromatography/mass spectrometry[34,35]. This is consistent with cholesterol in *C. elegans* only being required at low levels to generate various steroid hormones rather than as key component of membranes[36].

Quantitative lipid particle heterogeneity assessment.

To quantitatively assess the relative abundances of the different lipid particles, we developed an ensemble machine-learning analysis pipeline (see Methods for details). We first calculated 56 spectral and morphological descriptor metrics for each of the 10^4 lipid-rich particles we imaged. We then used a combination of clustering validation (NbClust[37]) and vertex component analysis[38] protocols that revealed the particles optimally grouped into two clusters, each having a canonical spectrum. One of these canonical spectra (extreme B) was essentially identical to the PLP spectra (inner product cosine similarity = 0.990 based on their spectra; 1.000 represents a perfect match). The other spectrum (extreme A) was essentially identical to the average spectra from the long-term dFA-retaining depots (inner product cosine similarity = 0.992). Being triglyceride-rich and protein-poor, this cluster probably functions in lipid storage (Supplementary Figs. 7a,b).

We used descriptors from these PLP and dFA-retaining datasets to train an ensemble classification system and attempted to classify each of the 10^4 lipid-rich particles as 'PLP-like' or 'lipid-storage'. Approximately 50% of particles were uniquely classified as belonging to either the PLP-like or lipid-storage groups. Linear regression analysis showed that the remaining particles were satisfactorily represented ($R^2 = 0.97 \pm 0.02$) as a mixture of the two extremes. These analyses indicated that about half of the lipid-rich particles in the intestine of adult *C. elegans* exist as intermediates between the triglyceride-rich particles (purple) and PLP-like particles (red) (Fig. 5a,c). Examples of typical spectra for the classified particles are shown in Fig. 5b. Intriguingly, we found a progression in the spatial distribution of the particles from the apical domain to the basolateral domain of the adult intestine: starting from the apical domain, first the distribution enriched in lipid-storage particles, then lipoprotein particles (intermediates) and finally PLPs (Fig. 5a and Supplementary Fig. 8a). The particle size also followed the same order, with the lipid-storage particles showing a broad size distribution with large average diameter (2.1 ± 0.9 μm) and the average size of both lipoprotein and PLP-like particles being relatively small (1.4 ± 0.7 and 1.2 ± 0.4 μm, respectively, Supplementary Fig. 8b).

We next examined the relative abundance of the two particle groups and intermediate mixtures (lipoprotein particles) in the early L4 and adult worms. Lipid-storage-type particles were the dominant lipid-rich particle in the early L4 intestine (>80%). In the adult intestine, the abundance of lipid-storage particles drops to ~45% of all lipid-rich particles, and that of

Author Manuscript Author Manuscript Author Manuscript Author Manuscript

lipoprotein particles increases from ~15% during the early L4 stage to ~50%, probably reflecting the biomass transformation of fat deposits in the mother worms to transitory lipoproteins. We found most of the lipid-rich particles in the gonad have characteristics of lipoprotein intermediates (>85%), with both lipid-storage and PLP-like particles representing minor populations(Fig.5d and Extended Data Fig. 1a). This is consistent with our earlier finding that most of the VIT-2::GFP signal within the oocytes is devoid of the lipid CARS signal (Supplementary Fig. 4c). In contrast, the less chemically dynamic lipid-rich particles in the epidermis were much more homogeneous, mostly classified as lipid-storage particles in both the early L4 and adult stages (>80%; Fig. 5d and Extended Data Fig. 1a). Taken together, these results suggest that the skin-like epidermis acts as a stable lipid storage site in *C. elegans*.

Finally, we examined *C. elegans* males because they do not synthesize yolk[30]. Most (>90%) of the lipid-rich particles in adult (*him-5*) male intestine were classified as lipid-storage particles (Fig. 5d and Extended Data Fig. 1b). The dearth of lipoprotein intermediates and PLP-like particles in males suggests that almost all of these abundant particles in the adult hermaphrodite intestine are related to yolk production.

Tissue-resolved starvation effects on lipid particles.

Further support for the notion that intestinal lipids of adult hermaphrodites are predominantly in the service of transferring nutrients to the developing oocytes came from application of our classifiers to intestinal lipids upon short-term starvation. Subjecting the gravid hermaphrodites to a short (2–3 h) fast resulted in only a modest decrease in intestinal lipid-rich particle density (from 379 ± 48 to 302 ± 33 particles per 4,000μm^2). During the same time frame, the population distribution among particle classes changed dramatically at the extremes: the lipid-storage population was halved and the PLP-like population increased fivefold, while the intermediate lipoprotein particle population remained mostly unchanged (Fig. 5d and Extended Data Fig. 1b). By contrast, the distribution of particle classes in gonad and epidermis remained similar in fed (Extended Data Fig. 1a and Fig. 5d) and short-term starved (Extended Data Fig. 1c and Fig. 5d) worms.

Because a short-term starvation did not result in an appreciable reduction in fat content of any of the examined tissues, we next examined conditions expected to do so. As our previous data had suggested that the dFA-retaining particles are probably lipid storage deposits (Fig. 4), we examined the effects on these particles of either long-term starvation (18–20 h) or exposure to phenformin, a drug known to activate AMPK leading to lipid catabolism[39]. Both conditions significantly decreased the intestinal and epidermal lipid contents (Extended Data Fig. 2a,b), resulting in a decreased number of dFA-retaining particles (Extended Data Fig. 2c). The intestinal fat was almost completely depleted (about <5% of the controls), while the fat level of epidermis was reduced to 10–25% of the controls (Extended Data Fig. 2b). By contrast, the oocytes retained their total lipid content and exhibited a substantial increase in the number of dFA-retaining particles (Extended Data Fig. 2a–c). Of the particles that remained in the intestine after either phenformin treatment or extended starvation, the vast majority were either lipoprotein or PLP-like particles, with very few triglyceride-rich lipid-storage particles observed (Extended Data Fig. 2a). Meanwhile,

Author Manuscript Author Manuscript Author Manuscript Author Manuscript

the remaining particle population of the epidermis and germline oocytes consisted of mostly the triglyceride-rich lipid-storage particles (epidermis) and lipoprotein particles (oocytes), where population distributions were similar to control animals (Extended Data Fig. 2a).

These observations are consistent with the epidermal lipid content probably serving as a long-term somatic energy reservoir and the intestinal deposits serving to transfer nutrient reservoirs to the germline oocytes during conditions of energetic challenge.

Discussion

Faced with the challenge of distinguishing among a heterogeneous population of lipid particles with distinct physiological functions, we leveraged the advantages of BCARS. We found that the lipid storage particles of *C. elegans* are relatively triglyceride-rich but protein-poor and exhibit slower lipid turnover rates compared to the lipoprotein particles of these animals. By analogy with mammalian lipoprotein biosynthesis, yolk generation may depend on a series of intermediate steps. Consistent with this, we found that that the intestines of adult hermaphrodites contain a continuum of intermediates between lipid storage and yolk particles. Significantly, at least 50% of the lipid-rich particles in the intestine of gravid animals are yolk-related lipoprotein particles. Even particles with the characteristics of lipid storage in the adult hermaphrodite intestines appear to be largely in the service of yolk production, at least in the context of fasting. Our findings suggest that following commitment to reproductive development, most of the intestinal lipid content is transitory in nature and destined to the progeny rather than being energy reservoirs for the parental somatic tissues. Although it represents a minor fraction of the overall fat content of *C. elegans*, nearly all of the lipid particles of the epidermis had characteristics of triglyceride-rich lipid storage depots that could be appropriately mobilized in response to energetic challenges (Fig. 6).

Our findings suggest the need for reinterpretation of all of the studies of *C. elegans* lipid metabolism and aging that have relied on intestine-dominated total fat measurements as a surrogate for assessing somatic adiposity. For example, the rapid loss of intestinal fat content observed following several hours of starvation has been interpreted as the oxidation of stored fats to meet the energetic demands of the parent hermaphrodite[22,40–42]. Our data suggest thata more likely possibility is that, in response to starvation, most intestinal lipids are preferentially transferred to the developing progeny, an outcome consistent with the known physiology of *C. elegans*.

In this work, we demonstrated that BCARS provides an unrivaled combination of label-free chemical specificity, imaging speed and spatial resolution for in vivo imaging. We believe that BCARS has the potential to be transformative to biological imaging, not only by allowing for acquisition of data from the relatively weak fingerprint region of Raman spectra but also by providing an intrinsically calibrated signal and absolute peak amplitudes[3] so that day-to-day imaging can be compared quantitatively. Furthermore, it is in principle possible to directly obtain species concentrations[43]. Finally, we expect machine-learning approaches to capitalize on the sample-invariant contrast and spatially resolved chemical specificity to discriminate between a range of biologically distinct states[44].

Author Manuscript
Author Manuscript
Author Manuscript
Author Manuscript

Online content

Any Nature Research reporting summaries, source data, extended data, supplementary information, acknowledgements, peer review information; details of author contributions and competing interests; and statements of data and code availability are available at https://doi.org/10.1038/s41589-020-0565-2.

Methods

Strains and reagents.

Wild-type (Bristol N2), CB4088 *him-5*(*e1490*) males, DH1390 *rme-2*(*b1008*), LIU1 *ldrIs1* [*dhs-3p*::*dhs-3*::*GF+unc-76*(+)] and a transgenic strain *bIs1*(*vit-2p*::*vit-2*::*GFP*) expressing a fusion of YP170 were used in this study. For the measurements of different developmental stages, synchronized worms were prepared via a two-generation egg lay method. For the first generation, ~10–20 adult worms were placed on the NGM OP50 plate and incubated at 20 °C for 2 h, and then the worms were removed. After an 80-h incubation at 20 °C, the laid eggs/embryos grew to gravid worms. Approximately 10–20 synchronized gravid worms were then picked and placed on the NGM OP50 plate and incubated at 20 °C for 2 h. After that, the gravid worms were removed and the synchronized embryos were incubated at 20 °C until appropriate stages for observation. This two-generation egg lay method can minimize the time error of synchronization, ensure more reproducible measurement results and avoid the starvation effect such as synchronization by L1 starvation arrest. The fixed LipidTOX staining of worms was carried out as previously described[22]. Phenformin was purchased from Sigma-Aldrich. Sodium azide was purchased from Sigma-Aldrich and used to anesthetize worms for microscopy.

Dietary supplementation of deuterium-labeled fatty acid and pulse-chase experiment.

NGM OP50 plates containing deuterium-labeled fatty acid (D33 oleic acid, Cambridge Isotope Laboratories) or fatty acid (oleic acid, Cayman Chemical) were prepared as previously described[17]. The final concentration of fatty acids was 1 mM. For the pulse-chase experiment, the synchronized late L4 worms (20–30 worms per plate) were placed on NGM OP50 plates containing fatty acids (oleic acid or deuterium-labeled oleic acid) and incubated at 20 °C for 12 h. After that, the worms were picked and placed on the normal NGM OP50 plates without deuterium and incubated at 20 °C for measurements at different time points.

BCARS/two-photon excitation fluorescence microscopy.

The set-up of the BCARS microscope is available in our previous report[7]. The current set-up, with spectrograph (Acton, SpectroPro2300i) and charge-coupled device camera (Andor, DU970N-FI), allowed us to collect BCARS (600–3,100 cm^{-1}) and two-photon excitation fluorescence microscopy (500–600 nm) signals simultaneously. The algorithms for Raman component retrieval from BCARS spectra (including Kramers–Kronig transfer, phase retrieval and baseline detrending) are described in our previous reports[7,8,10].

Author Manuscript

Author Manuscript

Author Manuscript

Author Manuscript

Workflow of ensemble machine-learning analysis.

The purpose of the machine-learning analysis was to determine whether all lipid-rich particles belong to a single group or were more appropriately represented by multiple groups. We took six discrete steps to determine this. In the first step we processed the collected BCARS data, retrieving Raman spectra for each pixel. From these spectra we determined which image pixels represent lipid-rich particles. Image and spectral data for these lipid-rich particles were analyzed in subsequent steps. In the second step we calculated a set of 56 spectral and morphological descriptor metrics for each of the 10^4 lipid-rich particles we imaged. These 56 descriptors are described in Supplementary Fig. 9. In the third step, we subjected these descriptors to each of the seven 'aggregation' functions found in NbClust[37], a widely used R library for cluster validation. The aggregation functions require the user to specify two additional parameters, one of six distance measures and one of 30 index types. When subjected to the particle descriptor metrics, each function/parameter combination yields a metric indicating the most likely number of distinct clusters in a dataset. These outcomes are of course subject to a set of assumptions implicit in the selection of the three function specifiers (aggregation function, distance measure and index type). Apart from expecting that the lipid-rich particle distribution could be continuous, we assumed no a priori knowledge of the distributions that would otherwise have led to favoring particular combinations of function specifiers. Given our lack of prior knowledge, we computed cluster number probabilities from each reasonable combination (7 aggregation functions × 5 distance measures × 16 index types). One distance measure could only be applied to binary data and 14 of the index types produced negative eigenvalues or did not converge. Results from each of these 560 independent calculations are aggregated in Supplementary Fig. 10, showing that two distinct clusters are most probable for our data.

The fourth step was to extract canonical spectra for the two putative clusters. For this we applied vertex component analysis[38] to the 10^4 particles we imaged (each particle has 56 descriptor metrics), assuming two extremes. The extreme (canonical) spectra that emerged from this analysis were essentially identical to the spectra of PLP particles and dFA-retaining particles previously identified. Accordingly, in the fifth step we used PLP and dFA-retaining particle descriptor metrics as input bases for bases for particle classification algorithms. The classification system was an ensemble approach incorporating linear support vector machines, decision trees and logistic regression[45], where the three classifier algorithms scored each lipid-rich particle and the final classification was determined by majority vote. In this way we trained two independent binary classification systems, one for specifically identifying lipid-storage and another for PLP-like particles. These were trained with the datasets containing dFA-retaining particles in the epidermis after a 24-h chase (lipid-storage particles) or PLP accumulation in *rme-2* adult worms (PLP-like particles), respectively. The training datasets contained ~10^3 particles, in which 80% were used for training and 20% were used for validation. The combined precision was ~90% for two binary classification systems.

The final step was to apply the two binary classification systems to each particle. At least 10^4 particles were classified, among them ~3.48% classified as PLP-like and 44.76% classified as lipid-storage. The remaining particles were not clearly classified in either of the

Author Manuscript

Author Manuscript

Author Manuscript

Author Manuscript

binary classes. However, we found that the descriptors of these non-binary class particles could be recapitulated as a linear combinationof the two canonical descriptor sets (R^2= 0.977±0.019,mean ±s.d.), suggesting that all lipid-rich particles were PLP, lipid-storage or an intermediate between the two extremes. The workflow is shown in Supplementary Fig. 9. Python, ImageJ and R programming were used for the data processing, image analysis and statistics.

Reporting Summary.

Further information on research design is available in the Nature Research Reporting Summary linked to this Article.

Data availability

The *C. elegans* accession codes (strains, developmental stages and sex) include the following: wild-type (Bristol N2), from L3 to gravid adult hermaphrodites; DH1390 *rme-2*(b1008), adult hermaphrodites; LIU1 *ldrls1* [*dhs-3p*::*dhs-3*::*GFP + unc76*(+)], adult hermaphrodites; CB4088 *him-5*(e1490), adult males; and a transgenic strain *bls1*(*vit-2p::vit-2::GFP*) expressing a fusion of YP170, adult hermaphrodites. Primary datasets generated and analyzed in this study consist of spectral image data. Each data file is in HDF5 format, and is ~5 GB in size. Approximately 50 such files were generated during the study. These data are available from the corresponding author on reasonable request. Intermediate data, such as spectral peak position and amplitude data extracted from spectral images after watershed, are also available upon request.

Code availability

Primary analysis of the coherent Raman spectra was performed using custom-built software that is publicly available and can be found at https://github.com/CCampJr/crikit2. Routine image analysis, such as watershed, was performed using Fiji ImageJ’s watershed method (v 1.52p, the latest version can be downloaded at https://imagej.net/Fiji). Statistical analysis was performed using NbClust (v 3.0), fitdistrplus (v 1.0–14) and ggplot2 (v 3.2.1) under R programming v 3.5.1, and SciKit-Learn (v 0.18.1) under Python v 3.4.

Author Manuscript

Author Manuscript

Author Manuscript

Author Manuscript

Extended Data

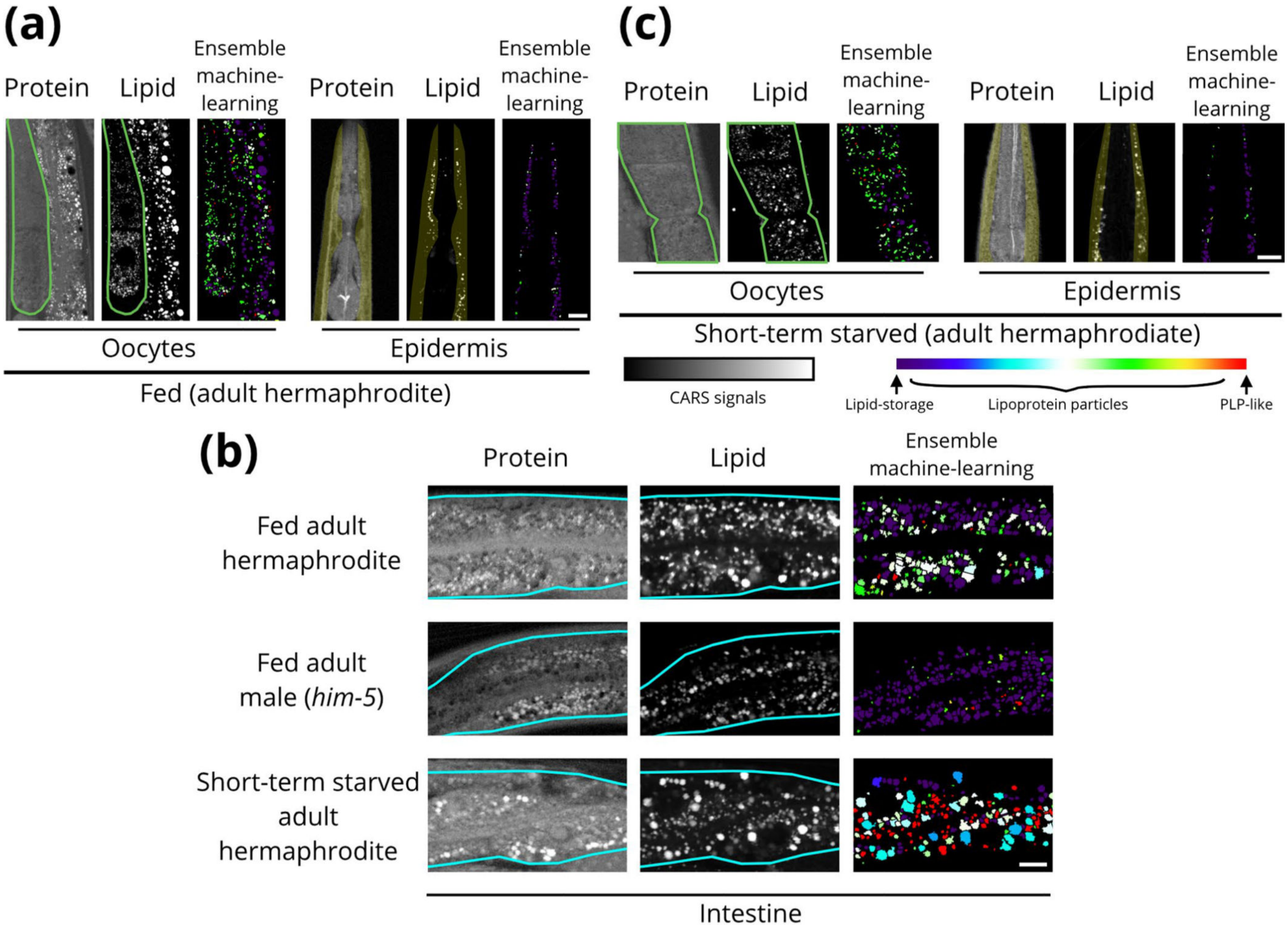

Extended Data Fig. 1 |. The analysis results after applying ensemble machine-learning method for fed and short-term starved (2–3 hr) adult hermaphrodites as well as adult male (*him-5*) worms

a, The analysis results of gonad (oocytes) and skin-like epidermis near pharynx in the fed wild-type adult hermaphrodites. **b**, The analysis results of the intestine in the fed / short-term starved adult hermaphrodite and male (*him-5*) worms. **c**, The analysis results of gonad and epidermis in the short-term starved adult hermaphrodites. Scale bar =10 μm for (**a**) to (**c**). The experiments were repeated at least four times independently with similar results for (**a**) and (**b**), and were repeated two times independently with similar results for (**c**). The region of pharyngeal neurons was excluded for the analysis of skin-like epidermis near pharynx.

Author Manuscript

Author Manuscript

Author Manuscript

Author Manuscript

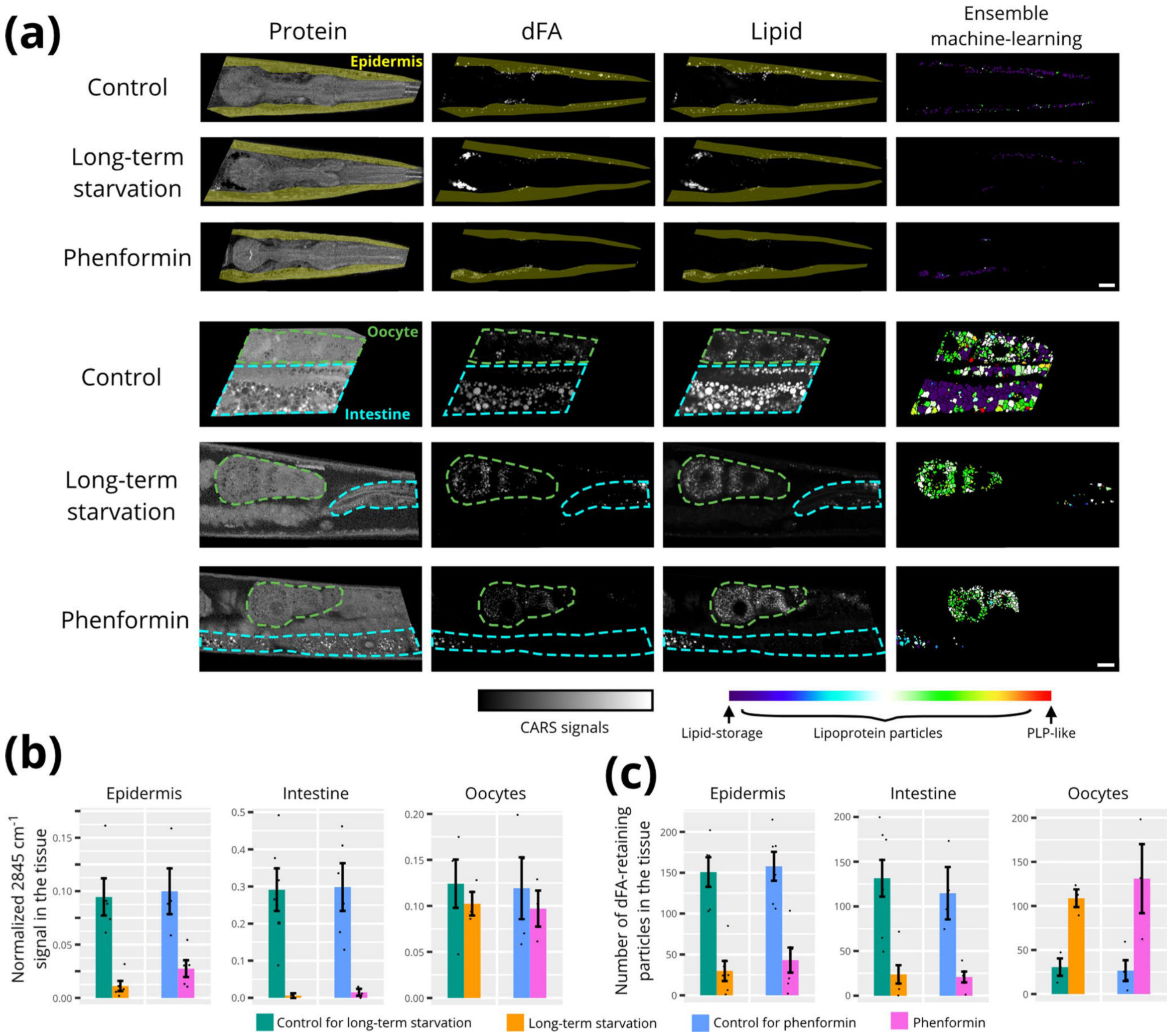

Extended Data Fig. 2 |. The effect of long-term starvation and phenformin

a, The CARS images of control, long-term starved (18–20 hr), and phenformin-treated worms. The young adult worms that had been fed dFA since the late L4 stage (12 h) were placed on the OP50 lawns that lacked the deuterium label (for control), on the plates lacked OP50 (for 18–20 h long-term starvation), and on the OP50 lawns that lacked the deuterium label but contained phenformin (20 h treatment with final concentration = 7.5 mM), respectively. After that, the worms were imaged by BCARS. The right column is the results after applied the ensemble machine-learning method. Scale bar =10μm. The experiments were repeated at least three times independently with similar results. The region of pharyngeal neurons was excluded for the analysis of skin-like epidermis near pharynx. **b**, The normalized lipid content (or normalized mean 2845 cm^{-1} intensity) of total lipid-rich particles in the tissue (normalized to a fixed tissue area). **c**, The average number of the dFA-retaining observed in the tissue (normalized to a fixed tissue area). Total ~4000 particles were analyzed; the data were collected from n=3–6 biologically independent animals for each condition, where each measurement is presented as a dot; The error bars represent the standard error of the mean.

Supplementary Material

Refer to Web version on PubMed Central for supplementary material.

Acknowledgements

K.A. and G.A.L. acknowledge support from NIH/NIA (R01AG046400) and BWF Innovations in Regulatory Sciences. T.C. acknowledges support from MOST-106-2119-M-001-030-MY3 of the Republic of China (Taiwan).

References

1. Delhaye M & Dhamelincourt P Raman microprobe and microscope with laser excitation. J. Raman Spectrosc. 3, 33–43 (1975).
2. Shipp DW, Sinjab F & Notingher I Raman spectroscopy: techniques and applications in the life sciences. Adv. Opt. Photon. 9, 315–428 (2017).
3. Camp CH Jr & Cicerone MT Chemically sensitive bioimaging with coherent Raman scattering. Nat. Photon. 9, 295–305 (2015).
4. Wang P et al. Imaging lipid metabolism in live Caenorhabditis elegans using fingerprint vibrations.Angew. Chem. Int. Ed. 53, 11787–11792 (2014).
5. Fu D et al. In vivo metabolic fingerprinting of neutral lipids with hyperspectral stimulated Raman scattering microscopy. J. Am. Chem. Soc. 136, 8820–8828 (2014). [PubMed: 24869754]
6. Shi L et al. Optical imaging of metabolic dynamics in animals. Nat. Commun. 9, 2995 (2018). [PubMed: 30082908]
7. Camp CH Jr et al. High-speed coherent Raman fingerprint imaging of biological tissues. Nat. Photon. 8, 627–634 (2014).
8. Liu Y, Lee YJ & Cicerone MT Broadband CARS spectral phase retrieval using a time-domain Kramers–Kronig transform. Opt. Lett. 34, 1363–1365 (2009). [PubMed: 19412273]
9. Freudiger CW et al. Label-free biomedical imaging with high sensitivity by stimulated Raman scattering microscopy. Science 322, 1857–1861 (2008). [PubMed: 19095943]
10. Camp CH Jr, Lee YJ & Cicerone MT Quantitative, comparable coherent anti-Stokes Raman scattering (CARS) spectroscopy: correcting errors in phase retrieval. J. Raman Spectrosc. 47, 408–415 (2016). [PubMed: 28819335]
11. Hellerer T et al. Monitoring of lipid storage in Caenorhabditis elegans using coherent anti-Stokes Raman scattering (CARS) microscopy. Proc. Natl Acad. Sci. USA 104, 14658–14663 (2007). [PubMed: 17804796]
12. Yen K et al. A comparative study of fat storage quantitation in nematode *Caenorhabditis elegans* using label and label-free methods. PLoS ONE 5, e12810 (2010). [PubMed: 20862331]
13. Le TT, Duren HM, Slipchenko MN, Hu C-D & Cheng J-X Label-free quantitative analysis of lipid metabolism in living *Caenorhabditis elegans*. J. Lipid Res. 51, 672–677 (2010). [PubMed: 19776402]
14. Klapper M et al. Fluorescence based fixative and vital staining of lipid droplets in *C. elegans* reveal fat stores using microscopic and flow cytometry approaches. J. Lipid Res. 52, 1281–1293 (2011). [PubMed: 21421847]
15. Wang MC, Min W, Freudiger CW, Ruvkun G & Xie XS RNAi screening for fat regulatory genes with SRS microscopy. Nat. Methods 8, 135–138 (2011). [PubMed: 21240281]
16. Li X et al. Quantitative imaging of lipid synthesis and lipolysis dynamics in *Caenorhabditis elegans* by stimulated Raman scattering microscopy. Anal. Chem. 91, 2279–2287 (2019). [PubMed: 30589537]

Author Manuscript

Author Manuscript

Author Manuscript

Author Manuscript

17. Chen WW et al. Specific polyunsaturated fatty acids modulate lipid delivery and oocyte development in *C. elegans* revealed by molecular-selective label-free imaging. Sci. Rep. 6, 32021 (2016). [PubMed: 27535493]
18. Srinivasan S Regulation of body fat in *Caenorhabditis elegans*. Annu. Rev. Physiol. 77, 161–178 (2015). [PubMed: 25340962]
19. Watts JL & Ristow M Lipid and carbohydrate metabolism in *Caenorhabditis elegans*. Genetics 207, 413–446 (2017). [PubMed: 28978773]
20. Watts JL Fat synthesis and adiposity regulation in *Caenorhabditis elegans*. Trends Endocrinol. Metab. 20, 58–65 (2009). [PubMed: 19181539]
21. Soukas AA, Kane EA, Carr CE, Melo JA & Ruvkun G Rictor/ TORC2 regulates fat metabolism, feeding, growth and life span in *Caenorhabditis elegans*. Genes Dev. 23, 496–511 (2009). [PubMed: 19240135]
22. O’Rourke EJ, Soukas AA, Carr CE & Ruvkun G *C. elegans* major fats are stored in vesicles distinct from lysosome-related organelles. Cell Metab. 10, 430–435 (2009). [PubMed: 19883620]
23. Perez MF & Lehner B Vitellogenins—yolk gene function and regulation in *Caenorhabditis elegans*. Front. Physiol. 10, 1067 (2019). [PubMed: 31551797]
24. Fukumoto S & Fujimoto T Deformation of lipid droplets in fixed samples. Histochem. Cell Biol. 118, 423–428 (2002). [PubMed: 12432454]
25. Lemieux GA & Ashrafi K Insights and challenges in using *C. elegans* for investigation of fat metabolism. Crit. Rev. Biochem. Mol. Biol. 50, 69–84 (2015). [PubMed: 25228063]
26. Vincent L & Soille P Watersheds in digital spaces: an efficient algorithm based on immersion simulations. IEEE Trans. Pattern Anal. Mach. Intell. 13, 583–598 (1991).
27. Hubbard EJ & Greenstein D Introduction to the Germ Line (WormBook, 2005); 10.1895/wormbook.1.18.1.
28. Dowen RH, Breen PC, Tullius T, Conery AL & Ruvkun G A microRNA program in the *C. elegans* hypodermis couples to intestinal mTORC2/PQM-1 signaling to modulate fat transport. Genes Dev. 30, 1515–1528 (2016). [PubMed: 27401555]
29. Grant B & Hirsh D Receptor-mediated endocytosis in the *Caenorhabditis elegans oocyte*. Mol. Biol. Cell 10, 4311–4326 (1999). [PubMed: 10588660]
30. Kimble J & Sharrock WJ Tissue-specific synthesis of yolk proteins in *Caenorhabditis elegans*. Dev. Biol. 96, 189–196 (1983). [PubMed: 6825952]
31. Zhang P et al. Proteomic study and marker protein identification of *Caenorhabditis elegans* lipid droplets. Mol. Cell. Proteom. 11, 317–328 (2012).
32. Schafer W Egg-laying (WormBook 2006); 10.1895/wormbook.1.38.1.
33. Czamara K et al. Raman spectroscopy of lipids: a review. J. Raman Spectrosc. 46, 4–20 (2015).
34. Kubagawa HM et al. Oocyte signals derived from polyunsaturated fatty acids control sperm recruitment in vivo. Nat. Cell Biol. 8, 1143–1148 (2006). [PubMed: 16998478]
35. Vrablik TL, Petyuk VA, Larson EM, Smith RD & Watts JL Lipidomic and proteomic analysis of *Caenorhabditis elegans* lipid droplets and identification of ACS-4 as a lipid droplet-associated protein. Biochim. Biophys. Acta Mol. Cell Biol. Lipids 1851, 1337–1345 (2015).
36. Kurzchalia TV & Ward S Why do worms need cholesterol? Nat. Cell Biol. 5, 684–688 (2003). [PubMed: 12894170]
37. Charrad M, Ghazzali N, Boiteau V & Niknafs A NbClust: an R package for determining the relevant number of clusters in a data set. J. Stat. Softw. 61, 1–36 (2014).
38. Nascimento JMP & Dias JMB Vertex component analysis: a fast algorithm to unmix hyperspectral data. IEEE Trans. Geosci. Remote Sens. 43, 898–910 (2005).
39. Sakamoto K, Göransson O, Hardie DG & Alessi DR Activity of LKB1 and AMPK-related kinases in skeletal muscle: effects of contraction, phenformin and AICAR. Am. J. Physiol. Endocrinol. Metab. 287, E310–E317 (2004). [PubMed: 15068958]
40. McKay RM, McKay JP, Avery L & Graff JM *C. elegans*: a model for exploring the genetics of fat storage. Dev. Cell 4, 131–142 (2003). [PubMed: 12530969]
41. O’Rourke EJ & Ruvkun G MXL-3 and HLH-30 transcriptionally link lipolysis and autophagy to nutrient availability. Nat. Cell Biol. 15, 668–676 (2013). [PubMed: 23604316]

Author Manuscript Author Manuscript Author Manuscript Author Manuscript

42. Lee JH et al. Lipid droplet protein LID-1 mediates ATGL-1-dependent lipolysis during fasting in *Caenorhabditis elegans*. Mol. Cell. Biol. 34, 4165–4176 (2014). [PubMed: 25202121]

43. Lee YJ, Moon D, Migler KB & Cicerone MT Quantitative image analysis of broadband CARS hyperspectral images of polymer blends. Anal. Chem. 83, 2733–2739 (2011). [PubMed: 21395296]

44. Hollon TC et al. Near real-time intraoperative brain tumor diagnosis using stimulated Raman histology and deep neural networks. Nat. Med. 26, 52–58 (2020). [PubMed: 31907460]

References

45. Hastie T, Tibshirani R & Friedman J The Elements of Statistical Learning. Data Mining, Inference and Prediction 2nd edn (Springer, 2009).

Author Manuscript Author Manuscript Author Manuscript Author Manuscript

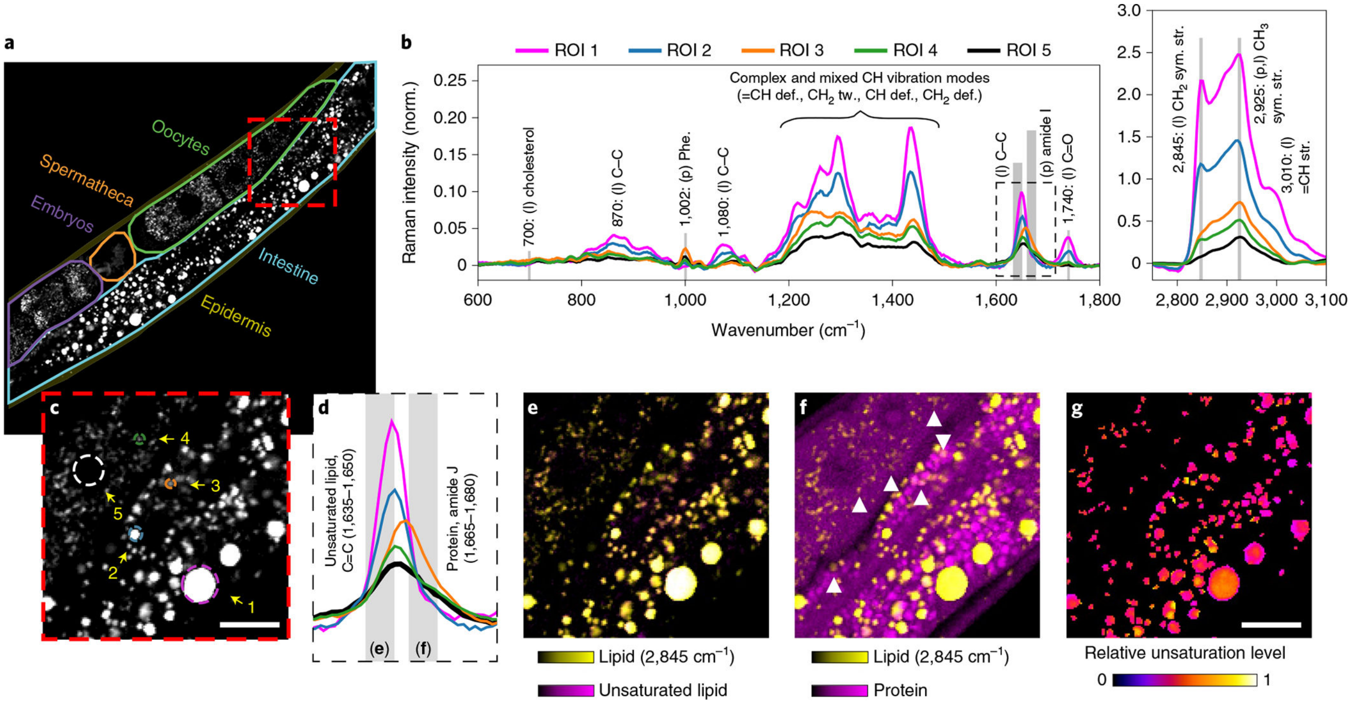

Fig. 1 |. Distinct chemical features of lipid-rich particles in *C. elegans*.

a, Lipid intensity map at 2,845 cm^{-1} and selected ROIs in a wild-type adult worm. The images in **c** and **e**–**g** correspond to the red box in **a**. **b**, Retrieved Raman spectra of the selected regions of interest (ROIs) shown in **c**. **c**, Selected ROIs 1–5, where ROI 5 is the oocyte nucleus that is lipid-poor. **d**, Expansion of the frequency region denoted by the dashed outline in **b**. **e**, Almost all the lipid-rich particles including ROIs 1–4 contain both a lipid signal (CH_2 stretching at 2,845 cm^{-1}, in yellow) and unsaturated fatty acids (C=C at 1,635–1,650cm^{-1}, in magenta). **f**, Some of the lipid-rich particles show a protein signal (amide I at 1,665–1,680cm^{-1}, in magenta), examples of which are indicated by arrowheads. **g**, Plot of the relative unsaturation level in lipid-rich particles using (normalized (1,635–1,650cm^{-1})/1,450cm^{-1}+normalized 3,010cm^{-1}/1,450cm^{-1})/2. The two ratios were normalized to the same pixel with the highest ratio. Raman band: 1,450cm^{-1} for C–C stretching and 3,010cm^{-1} for =C–H stretching. Scale bars in **c** and **g**, 10μm.The same scale bar applies to **e** and **f**. The experiments were repeated at least three times, independently, with similar results.

Author Manuscript

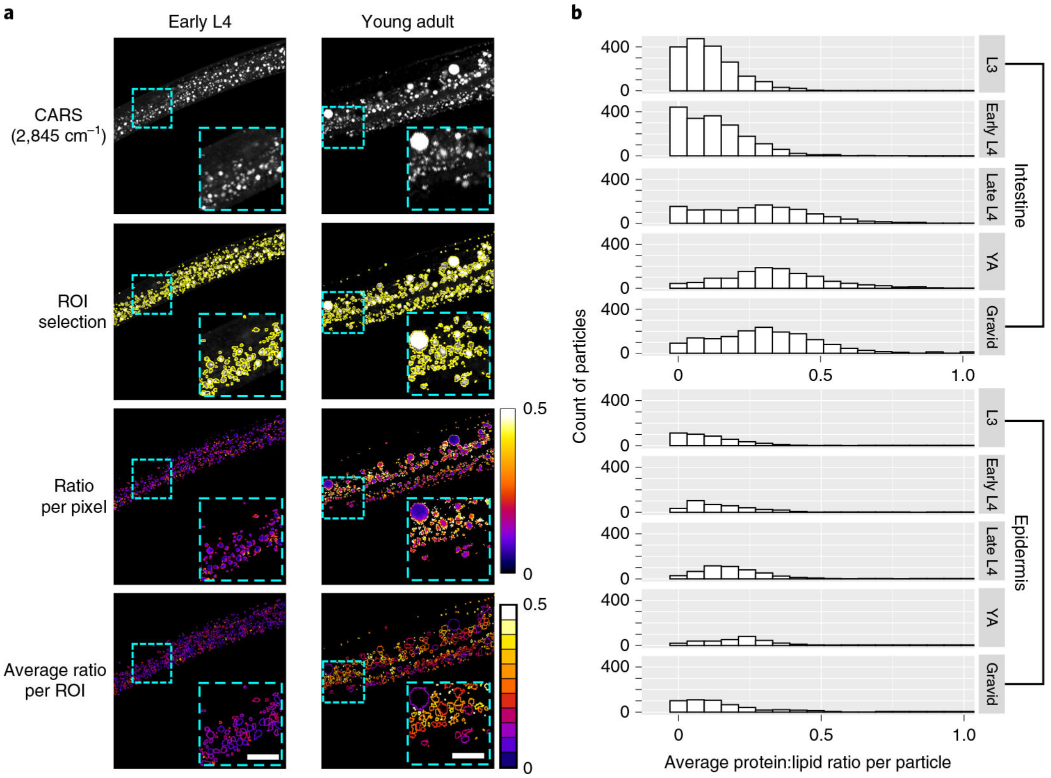

Fig. 2 |. Ratiometric BCARS imaging of *C. elegans*.

a, Protein:lipid ratio (integrated 1,665 to 1,680cm^{-1}/2,845 cm^{-1}) heat mapping of early L4 and young adult wild-type *C. elegans* hermaphrodites. Scale bars, 10µm. The experiments were repeated at least five times, independently, with similar results. **b**, Histogram distribution of average protein:lipid ratio at different developmental stages. From L3 to gravid developmental stages, n = 10, 8, 6, 6 and 6 biologically independent animals for the intestine and n=9,6, 10,8 and 8 biologically independent animals for the epidermis near the pharynx, respectively. Approximately 1,200–1,800 intestinal particles and 300–500 epidermal particles were quantified for each stage.

Author Manuscript

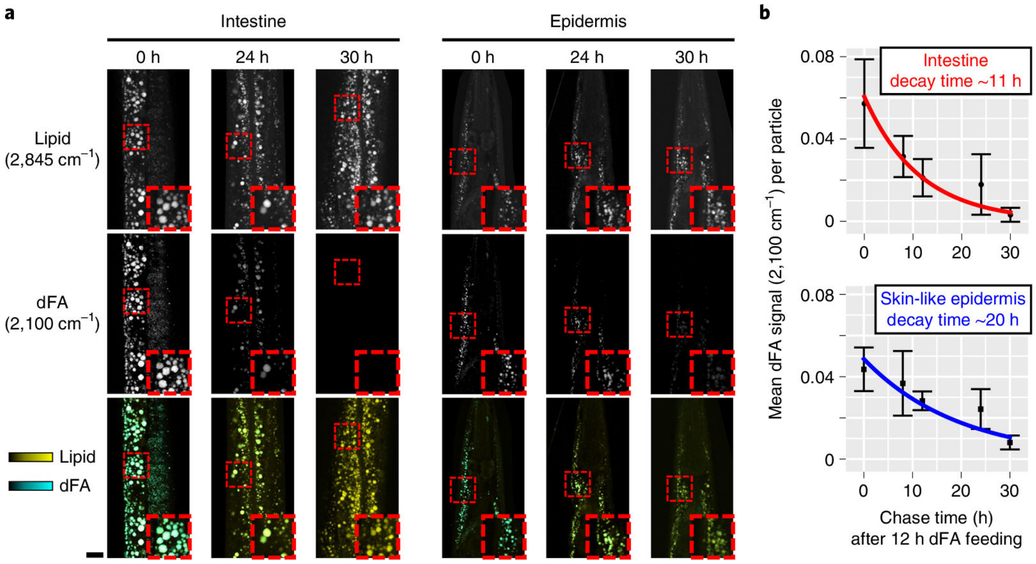

Fig. 3 |. Pulse-chase analysis of assimilated dFA.

Young adult *C. elegans* that had been fed with dFA for 12 h were placed on *E. coli* plates lacking dFA and examined at different chase times. **a**, CARS images of total lipids and dFA in the intestine and skin-like epidermis near the pharynx. The images in the third row are overlaid images of 2,845 cm^{-1} (yellow) and 2,100 cm^{-1} (cyan) images. Scale bar, 10μm. At a chase time of 24h, 86%of 716 epidermal lipid-rich particles identified exhibited a C–D label signal above baseline (average 2,100-cm^{-1} intensity of >0.01). These values were derived from three independent experiments on separate animals. **b**, The digested dFA dissipating time (exponential decay time of the average dFA signal) for the intestine and skin-like epidermis. For chase times of 0, 8, 12, 24, 30 h, the total numbers of intestinal lipid-rich particles were 388, 293, 1,669, 634 and 875, and the total numbers of epidermal particles were 162, 160, 236, 211 and 254, respectively. The data at each time point were obtained from $n = 3$ biologically independent animals. The center points represent mean values and the error bars represent s.d.

Author Manuscript

Author Manuscript

Author Manuscript

Author Manuscript

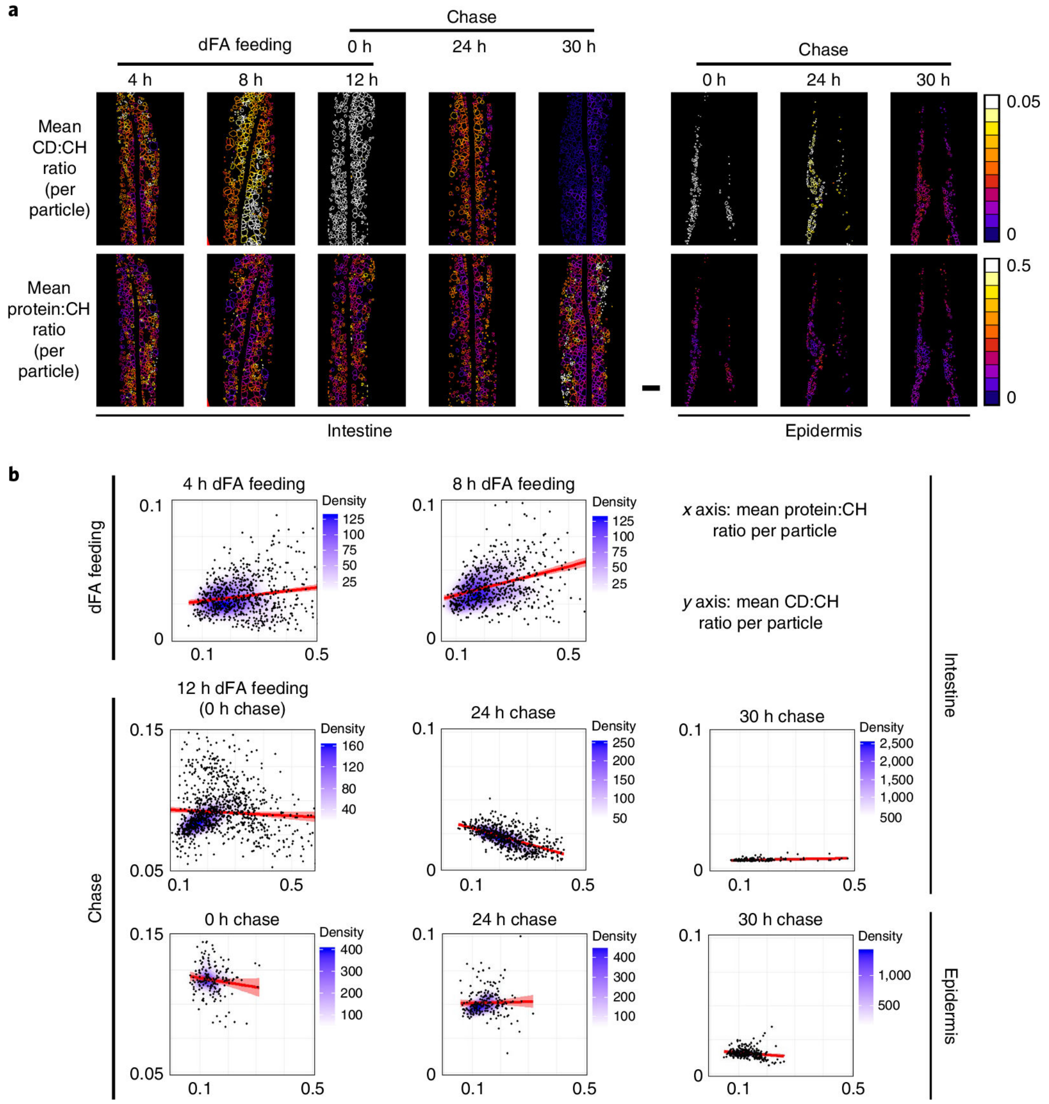

Fig. 4 |. Correlation between CD:CH (2,100 cm^{-1}/2,845 cm^{-1}) and protein:CH (1,665–1,680 cm^{-1}/2,845 cm^{-1}) ratios.

a, Heat maps of the CD:CH and protein:CH ratios in the intestine and epidermis. Scale bar, 10μm. The experiments were repeated three times, independently, with similar results. **b**, Density scatter plots of the correlations between CD:CH and protein:CH ratios at different dFA feeding or chase time points. The total numbers of intestinal lipid-rich particles were 810 for 4 h dFA feeding, 644 for 8 h dFA feeding, 1,010 for 12-h dFA feeding (or 0 h chase), 634 for 24 h chase and 876 for 30 h chase. The total numbers of epidermal lipid-rich particles were 162 for the 0 h chase, 211 for 24 h chase and 254 for 30 h chase. The data at each time point were obtained from $n = 3$ biologically independent animals. The line and shading in the graph represent the linear regression and 95% confidence interval, respectively. The Pearson correlation coefficients (r) are 0.13 and 0.35 (4 h and 8 h dFA feeding, intestine); -0.08, -0.7 and -0.69 (0 h, 24 h and 30 h chase, intestine); -0.13, 0.2 and -0.18 (0 h, 24 h and 30 h chase, epidermis).

Author Manuscript

Author Manuscript

Author Manuscript

Author Manuscript

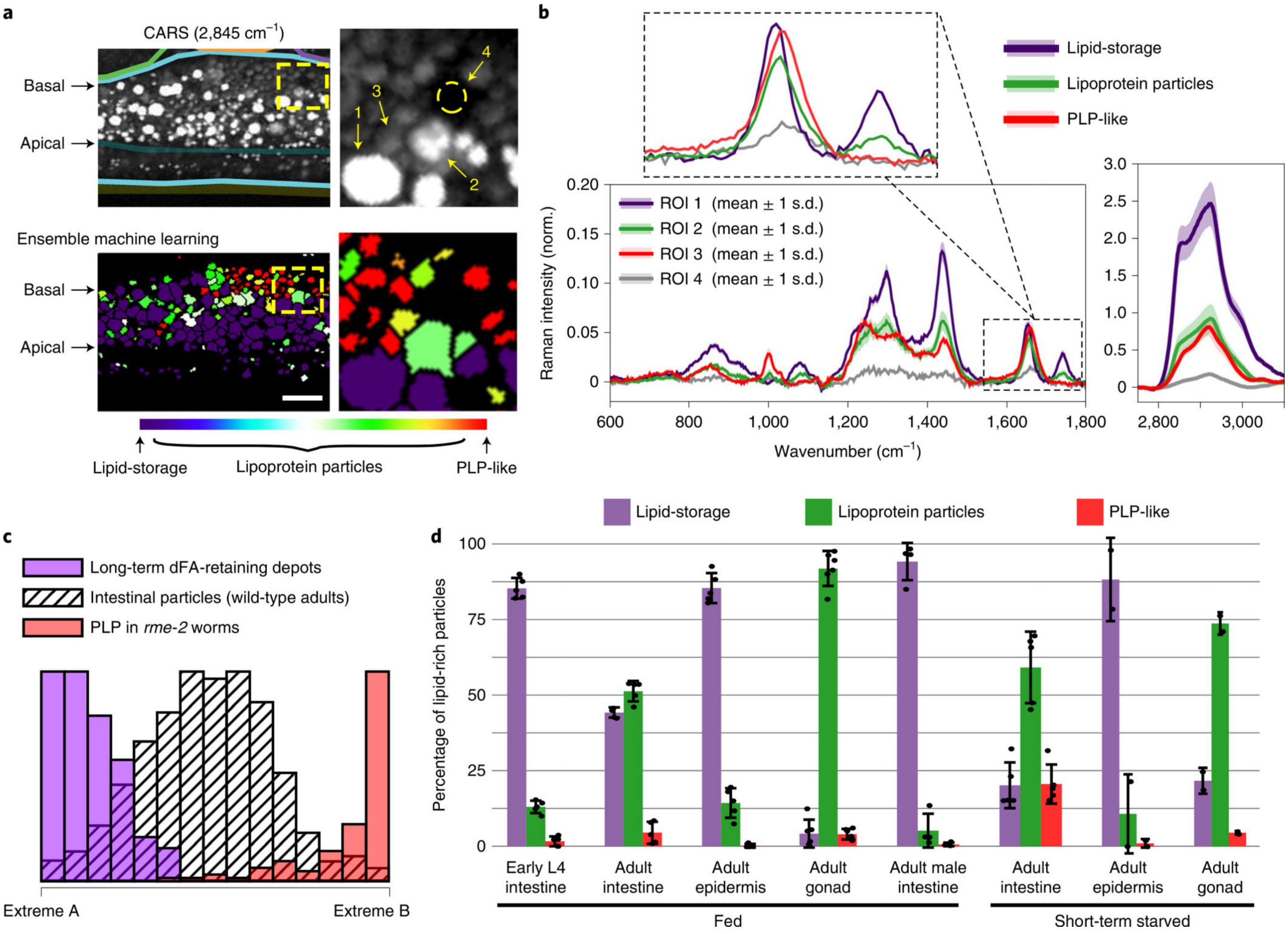

Fig. 5 |. Characterization of lipid-rich particles in *C. elegans* with the ensemble machine-learning method.

a, CARS (2,845 cm^{-1}) image and the result after applying the ensemble machine-learning method. In the image of ensemble machine learning, purple represents lipid-storage particles, red represents PLP-like particles, and the coded colors for lipoprotein particles represent the fraction of lipid-storage and PLP-like components. Scale bar, 10μm.The panels on the right are expansions of the regions enclosed by dashed yellow boxes. **b**, Retrieved Raman spectra of the regions of interest (ROIs) indicated in **a**. The lines and shading represent the mean values and 1s.d. of the pixel intensities in the ROI. **c**, Histogram of long-term dFA-retaining depots in the epidermis (lipid-storage particles, purple), PLP in *rme-2* (red) and pooled data of intestinal lipid-rich particles in wild-type adult worms (hashed pattern, *n*=5)after applying linear regression based on the spectra of two extremes shown in Supplementary Fig.7b. **d**, Average percentage of two particle classes (lipid-storage and PLP-like) and intermediate mixtures (lipoprotein particles) in early L4 intestine, adult intestine, adult epidermis and adult gonad of fed hermaphrodites as well as the intestine of fed adult males (*him-5*) are shown. For short-term (2–3 h) starvation, average percentages of the particles in the adult intestine, epidermis and gonad of hermaphrodites are shown. Error bars represent s.d. Each measurement is presented as a dot. *n*=5 biologically independent animals for fed hermaphrodite tissues including early L4 intestine, adult intestine and adult epidermis; *n*=6 biologically independent animals for fed adult gonad; *n*=4 biologically independent animals for male adult (*him-5*); *n*=5 biologically independent animals for short-term starved adult intestine; *n*=2 biologically independent animals for short-term starved adult epidermis and gonad. Approximately 10^4 particles were classified in total.

Author Manuscript Author Manuscript Author Manuscript Author Manuscript

Author Manuscript

Author Manuscript

Author Manuscript

Author Manuscript

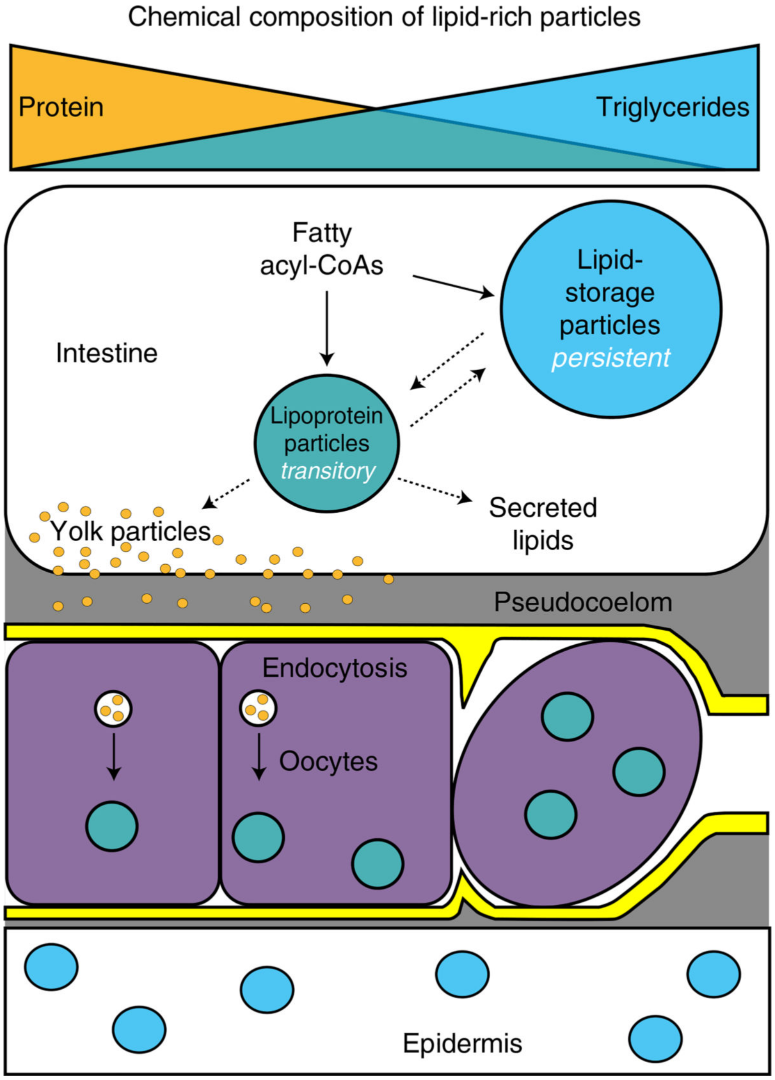

Fig. 6 |. *C. elegans* hermaphrodite lipid-rich particles encompass a continuum of chemical compositions and lifetimes, which vary with tissue localization and reproductive capacity.
The oocytes are bounded by basal laminae (sheath cells in yellow).